

**OPEN ACCESS**

## Multi-Scale Simulation of Heterogeneous Surface Film Growth Mechanisms in Lithium-Ion Batteries

To cite this article: Fridolin Röder *et al* 2017 *J. Electrochem. Soc.* **164** E3335

View the [article online](#) for updates and enhancements.

### You may also like

- [Multi-Scale Study of Branched Electrodeposits](#)  
Chams Kharbachi, Fabien Chauvet and Theo Tzedakis
- [Oxidation Kinetics of Cobalt Diffusing out of High Current Density \(HCD\) Plated Gold](#)  
J. H. Thomas
- [Focus on Quantum Gases](#)  
Murray J Holland



 **Connect with decision-makers at ECS**

Accelerate sales with ECS exhibits, sponsorships, and advertising!

▶ Learn more and engage at the 244th ECS Meeting!



## Multi-Scale Simulation of Heterogeneous Surface Film Growth Mechanisms in Lithium-Ion Batteries

Fridolin Röder,<sup>a,b</sup> Richard D. Braatz,<sup>c</sup> and Ulrike Krewer<sup>a,b,z</sup>

<sup>a</sup>Institute of Energy and Process Systems Engineering, TU Braunschweig, 38106 Braunschweig, Germany

<sup>b</sup>Battery LabFactory Braunschweig, TU Braunschweig, 38106 Braunschweig, Germany

<sup>c</sup>Massachusetts Institute of Technology, Cambridge, Massachusetts 02319, USA

A quantitative description of the formation process of the solid electrolyte interface (SEI) on graphite electrodes requires the description of heterogeneous surface film growth mechanisms and continuum models. This article presents such an approach, which uses multi-scale modeling techniques to investigate multi-scale effects of the surface film growth. The model dynamically couples a macroscopic battery model with a kinetic Monte Carlo algorithm. The latter allows the study of atomistic surface reactions and heterogeneous surface film growth. The capability of this model is illustrated on an example using the common ethylene carbonate-based electrolyte in contact with a graphite electrode that features different particle radii. In this model, the atomistic configuration of the surface film structure impacts reactivity of the surface and thus the macroscopic reaction balances. The macroscopic properties impact surface current densities and overpotentials and thus surface film growth. The potential slope and charge consumption in graphite electrodes during the formation process qualitatively agrees with reported experimental results.

© The Author(s) 2017. Published by ECS. This is an open access article distributed under the terms of the Creative Commons Attribution 4.0 License (CC BY, <http://creativecommons.org/licenses/by/4.0/>), which permits unrestricted reuse of the work in any medium, provided the original work is properly cited. [DOI: 10.1149/2.0241711jes] All rights reserved.



Manuscript submitted March 29, 2017; revised manuscript received May 11, 2017. Published June 3, 2017. *This paper is part of the JES Focus Issue on Mathematical Modeling of Electrochemical Systems at Multiple Scales in Honor of John Newman.*

A long lifetime for lithium-ion batteries is key to reducing battery cost and increasing acceptance for new applications. The most important but still not well understood aging phenomenon is the growth of a solid film at graphite negative electrodes.<sup>1–3</sup> Graphite is the common negative electrode and operates at conditions outside the electrochemical stability window of the electrolyte.<sup>2,4</sup> Its decomposition takes place at the surface of the electrode particles and leads to the formation of a surface film, i.e. solid electrolyte interface (SEI). The SEI is mainly built during the first cycles prior to use and is considered to be part of the manufacturing process.<sup>5</sup> The aim of the formation process is to create an interface that is a good lithium-ion conductor but insulating for electrons and prohibits direct contact between electrode and electrolyte in order to provide good performance and long lifetime.<sup>4</sup> Different compositions of the film have been proposed by different research groups.<sup>6,7</sup> Since the composition and structure and so the film characteristic is determined during the first cycles,<sup>7</sup> a detailed understanding of this growth mechanism is needed to improve cycling performance.

The SEI is formed by a complex mechanism.<sup>5</sup> An atomistic reaction mechanism involves lithium salt and solvent as reactants as well as a variety of different organic and inorganic intermediates and solid products.<sup>7,8</sup> The observation of the formation process is challenging, because of the film's thickness of only several nanometers. Additionally, macroscopic properties such as particle size or operating conditions, e.g. C-rate and environmental temperature, have an important impact on the formation process.<sup>3,4</sup> Although SEI film formation has been studied for decades using experimental and simulation-based methods, the exact mechanism of chemical and electrochemical reactions and the growth of the solid film is not understood. Indeed, Kalz et al.<sup>9</sup> pointed out the general need for a deeper analysis and advanced modeling of changes of reactive surfaces. New modeling methods need to be explored, which allow application to lithium-ion batteries for a detailed simulation of heterogeneous growth mechanisms while considering the experimentally found impact of macroscopic properties.

Several model-based approaches have been proposed for studying the SEI. Models are available at different scales based on molecular dynamics (MD), density functional theory (DFT), kinetic Monte Carlo (kMC), and partial differential equations (PDEs). MD simulations have been used to determine and analyze basic atomistic

processes<sup>6,10,11</sup> and usually assume ideal surfaces or solutions. DFT has been applied to determine energy barriers and standard state potentials<sup>12</sup> and transport processes in the solid film.<sup>13,14</sup> Methekar et al.<sup>15</sup> proposed the application of kMC to simulate heterogeneous passivation of the interface. Several macroscopic electrode models are available based on PDEs to simulate film growth and resistance<sup>16,17</sup> and for detailed analysis of transport processes and reactions in the SEI.<sup>18</sup> Most atomistic methods can only be applied on very short time and length scales and cannot simulate the long time scale formation process in an electrode. On the other hand, homogeneous macroscopic methods do not consider process heterogeneity due to lateral interaction of species on a higher dimensional surface, which results in the complex structures observed experimentally. Using kMC method in combination with macroscopic continuum equations has been shown to be a promising approach for analysis of multi-scale problems in other electrochemical systems, such as fuel cells<sup>19</sup> and copper electrodeposition.<sup>20</sup> To enable understanding the complex film formation mechanisms in lithium-ion batteries in future, this article introduces an advanced modeling methodology that couples heterogeneous surface reactions and film growth mechanisms with a macroscopic single-particle electrode model using multi-scale modeling.

This multi-scale modeling approach is an extension of a conference paper that outlined the basic steps.<sup>21</sup> After explaining the approach, we qualitatively validate its ability to simulate key aspects of the formation process, such as the SEI formation plateau. The method is demonstrated by simulating the formation process for electrolyte with a pure ethylene carbonate (EC) solvent, which is known to form a stable film on the surface. As its exact mechanism is still not fully understood,<sup>22</sup> the scope of this work is not a fully validated simulation, but to provide a computational tool for the testing of hypothesized mechanisms that can be compared with experimental data and used for analysis of multi-scale behavior.

### Mathematical Modeling

In this work, a macroscopic electrode model based on mass and charge balances is dynamically coupled with a kinetic Monte Carlo model covering heterogeneous surface film growth mechanisms. The individual models can also be used without the coupling algorithm and have been evaluated separately in preliminary steps. The multi-scale model and the various phases considered are illustrated in Figure 1. It can be seen that the electrode is represented as a single electrode

<sup>z</sup>E-mail: u.krewer@tu-braunschweig.de

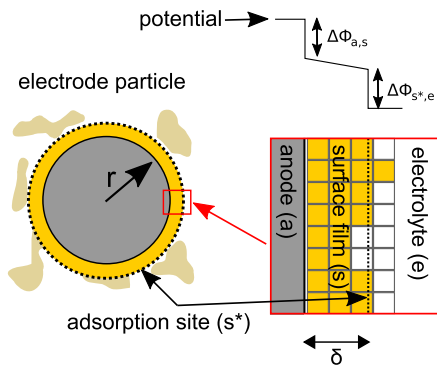


**Figure 1.** Multi-scale model showing electrode represented as a single electrode particle covered by a dense inner surface film (s) and further solid degradation products in the electrolyte reducing the porosity. A zoom into the film structure is indicated by a red square. Further, electric potential drop from anode (a) through surface film (s) and adsorption site (s\*) to electrolyte (e) is illustrated.

particle covered by a dense inner surface film (s) and further solid degradation products in the electrolyte reducing the porosity. Processes on this scale are considered by the macroscopic model. A zoom into the film structure is indicated by a red square. Processes on this scale are considered by the atomistic model using kMC method. The surface film thickness  $\delta$  is the average film thickness and is determined by the atomistic model. Further, electric potential drop from anode (a) through surface film (s) and adsorption site (s\*) to electrolyte (e) is illustrated. In Macroscopic scale section and Atomistic scale section the macroscopic and atomistic model and their general equations are introduced, respectively. In Multi-scale coupling section the coupling of both models is explained. Finally, in Example problem: SEI layer formation in ethylene carbonate electrolyte section the methodology is applied to a particular example problem for EC decomposition on graphite electrodes.

**Macroscopic scale.**—The macroscopic model considers mass and charge conservation, transport processes through SEI and active material particles, as well as kinetic limitations, i.e., charge transfer reactions. All phases shown in Figure 1 are involved, which are: anode (a), surface film (s), adsorption site (s\*), and electrolyte (e).

The model is based on a single-particle model approach similar to that of Santhanagopalan et al.<sup>23</sup> and is extended by SEI based on the work of Colclasure et al.<sup>18</sup> Diffusion of lithium in the solid phase of the negative electrode, i.e. anode *a*, is modeled as

$$\frac{\partial c_a^{\text{Li}}(r)}{\partial t} = \frac{1}{r^2} \nabla (D_a^{\text{Li}} r^2 \nabla c_a^{\text{Li}}(r)) \quad [1]$$

where  $c_a^{\text{Li}}$  is the lithium concentration,  $r$  the radial dimension, and  $D_a^{\text{Li}}$  the solid diffusion coefficient in the anode. The boundary conditions are  $-D_a^{\text{Li}} \nabla c_a^{\text{Li}}(0) = 0$  and  $-D_a^{\text{Li}} \nabla c_a^{\text{Li}}(R_a) = N_{a,s}^{\text{Li}^+} r_s$ , with particle radius  $R_a$  and lithium reaction rate  $N_{a,s}^{\text{Li}^+}$  at the interface between anode and surface film and surface roughness factor  $r_s$ . The SEI is a surface film, which encloses the active material particle and is conductive only for lithium ions. The surface film is assumed to be planar, since its thickness is orders of magnitude smaller than that of the particle radius. Further, the SEI is treated as a single ion conductor with assumed electroneutrality, which denotes constant lithium concentration in the SEI and enforces equal flow rates for lithium through the *a/s* and *s/s\** interfaces. Therefore, reactions for lithium passing those interfaces are treated as a homogeneous reaction in series as explained by Helfreich,<sup>24</sup> which allows the elimination of intermediate concentrations in the SEI phase *s* and determination of overall forward and backward rates  $N_{a,s}^{\text{Li}^+}$  and  $N_{s,s^*}^{\text{Li}^+}$  from phase *a* to phase *s\** as

$$N_{a,s}^{\text{Li}^+} = N_{s,s^*}^{\text{Li}^+} = \frac{\Gamma}{\sigma} \left( a_a^{\text{Li}}(R_a) \frac{\lambda_{a,s} \lambda_{s,s^*}}{\lambda_{s,a} + \lambda_{s,s^*}} - \theta_{s^*}^{\text{Li}^+} \frac{\lambda_{s,a} \lambda_{s^*,s}}{\lambda_{s,a} + \lambda_{s,s^*}} \right) \quad [2]$$

$$\lambda_{a,s} = k_{10}^f \exp\left(\frac{-E_{10}^A + \alpha_{10} \Delta \Phi_{a,s} F}{RT}\right) \quad [3]$$

$$\lambda_{s,a} = k_{10}^b a_a^V(R_a) \exp\left(\frac{-E_{10}^A - (1 - \alpha_{11}) \Delta \Phi_{a,s} F}{RT}\right) \quad [4]$$

$$\lambda_{s,s^*} = k_{11}^f \theta_{s^*}^V \exp\left(\frac{-E_{11}^A}{RT}\right) \quad [5]$$

$$\lambda_{s^*,s} = k_{11}^b \exp\left(\frac{-E_{11}^A}{RT}\right) \quad [6]$$

with surface fraction  $\theta^{\text{Li}^+}$  of lithium, site occupancy number  $\sigma$ , site density  $\Gamma$ , and activity of lithium  $a_a^{\text{Li}}$  and vacancies  $a_a^V$  in the anode, which are determined as a function of concentration  $c^{\text{Li}^+}$  based on Redlich Kister coefficients for graphite provided by Colclasure et al.<sup>25</sup>

At the adsorption site *s\** of the film, balance equations for considered species *j* are applied as

$$\frac{\Gamma}{\sigma} \frac{\partial \theta^j}{\partial t} = N_{s,s^*}^j + N_{s^*,e}^j + \sum v^j Q^j \quad [7]$$

with flow rates through interfaces  $N^j$ , source terms through reactions on the adsorption site  $Q^j$ , and stoichiometric factor  $v^j$ . Those terms can be specified by continuum equations as shown by Colclasure et al.<sup>18</sup> or be a result of atomistic simulations as given in the Multi-scale coupling section.

Charge balance equations are applied for the interfaces between anode/surface film *a, s* and adsorption site/electrolyte *s\*, e* as

$$a_s^{\text{eff}} C_{a,s}^{\text{DL}} \frac{\partial \Delta \Phi_{a,s}}{\partial t} = -j^{\text{charge}} + j_{a,s}^{\text{ct}} \quad [8]$$

and

$$a_{s^*,e}^{\text{eff}} C_{s^*,e}^{\text{DL}} \frac{\partial \Delta \Phi_{s^*,e}}{\partial t} = -j^{\text{charge}} + j_{s^*,e}^{\text{ct}} \quad [9]$$

with the potential difference at the interface  $\Delta \Phi$ , applied charge density  $j^{\text{charge}}$ , charge transfer reaction current  $j^{\text{ct}}$ , double layer capacitance  $C^{\text{DL}}$ , and specific effective surface area of a rough particle,  $a_s^{\text{eff}} = \frac{3r_s \epsilon_a}{R_a}$ . Charge transfer reaction current is the sum of charge transferred at this interface. The electrical potential drop in the surface film is determined as

$$\Delta \Phi_s = \frac{j^{\text{charge}} \rho_{\text{SEI}} \delta}{a_s^{\text{eff}}} \quad [10]$$

with electrical resistivity of the SEI,  $\rho_{\text{SEI}}$ , and the average film thickness  $\delta$ . The electrode potential  $\Delta \Phi_{\text{electrode}}$  is then determined as

$$\Delta \Phi_{\text{electrode}} = \Delta \Phi_{a,s} + \Delta \Phi_{s^*,e} + \Delta \Phi_s \quad [11]$$

**Atomistic scale.**—Whereas a macroscopic model is very limited to describe heterogeneous surface film growth processes, kMC is an adequate method.<sup>15</sup> Proposed mechanisms of decomposition of electrolytes at the SEI are often highly complex, where most of the reactants are not simple atoms but molecules with complex structures. The film formation is usually performed in a time period of several hours. Such a long time scale, however, can presently barely be realized by first-principles kMC simulation considering every possible transition state on the atomistic scale without further simplifications. In consideration of this, the aim of applying kMC in this article is not to propose a first-principles calculation to accurately predict the formation processes, but rather to provide a methodology to introduce selected heterogeneous processes of interest into commonly used continuum-only battery models.

The kMC model is based on the solid-on-solid approach.<sup>26–28</sup> In contrast to a 3D model, this kMC model allows adsorption only on top of surface sites, which avoids overhangs and is a good approximation

as long as difference of height between neighboring sites is not exceedingly large.<sup>28</sup> The kMC algorithm is based on examples provided by Burghaus.<sup>29</sup> A cubic lattice is used, with diagonal and horizontal diffusion allowed.

The area of the lattice is:

$$A^{\text{kMC}} = n_z n_y (\Delta L)^2 \quad [12]$$

where  $n_z$  and  $n_y$  are the numbers of lattice sites in  $z$  and  $y$  direction, respectively. The distance between two lattice sites is  $\Delta L$ .

The implemented processes are surface diffusion, adsorption, desorption, and reactions. Interface processes with phase change, such as electrochemical reaction, adsorption, and desorption can be anodic, cathodic, or neutral, i.e. with uncharged species. Process frequency  $q$  are implemented as an Arrhenius equation

$$q = k \exp\left(\frac{-E^A}{RT}\right) \quad [13]$$

with activation energy  $E^A$ . For electrochemical reactions, further dependency of the applicable electrical potential  $\Delta\Phi$  is considered as

$$q = k \exp\left(\frac{-E^A + \alpha\Delta\Phi F}{RT}\right) \quad [14]$$

Diagonal and horizontal surface diffusion pre-exponential factors are determined based on the surface diffusion coefficient  $D$ , with pre-exponential factor being  $k^{\text{diff}} = w^h = \frac{D}{2(\Delta L)^2}$  for the horizontal diffusion and  $k^{\text{diff}} = w^d = \frac{D}{4(\Delta L)^2}$  for diagonal diffusion.<sup>26</sup> The activation energy for diffusion or desorption steps depends on the bonds to nearest neighbor sites and can be expressed as  $E^A = \sum_j n_j J_j^A$ , where  $n_j$  is the number and  $J_j^A$  is the bonding energy to a neighbor of type  $j$ .<sup>27</sup> The adsorption rate depends on the species activity in the electrolyte  $a_e$ . Some of the reactions involve electrons, which are present at the electrode surface; those electrochemical reactions are driven by the potential difference between anode  $a$  and the adsorption site  $s^*$ . Furthermore, electrons need to pass the surface film and thus reaction rates decrease with increasing film thickness. The electron leakage process is not fully understood. Even so, some suggestions are given in the literature.<sup>13,14,30,31</sup> In this work, we assume that an electron needs to overcome an additional activation energy  $E_{\text{SEI}}^A$ , which depends on the distance  $\delta^{\text{kMC}}$  between local surface site and the anode as

$$E_{\text{SEI}}^A = \delta^{\text{kMC}}(z, y) \bar{E}_{\text{SEI}}^A \quad [15]$$

where  $\bar{E}_{\text{SEI}}^A$  is the specific activation energy. As such, the reaction rate exponentially decreases with increasing surface film thickness. This dependency is commonly assumed in macroscopic models.<sup>32</sup> The specific activation energy  $\bar{E}_{\text{SEI}}^A$  is thereby a parameter that is chosen to achieve a reasonable film thickness. Reverse rates of processes in this model as well as in the macroscopic model are determined based on the standard chemical potentials of the species, by calculating the change of Gibbs free energy  $\Delta G^0 = \sum \mu_{\text{products}}^0 - \sum \mu_{\text{educts}}^0$ ,<sup>25</sup> which can then be further used to determine the backward reaction rates from

$$\frac{k^f}{k^b} = \exp\left(\frac{-\Delta G^0}{RT}\right) \quad [16]$$

As mentioned previously, the kMC simulations are used to introduce heterogeneous surface processes into a continuum model. As such, only particular species of interest are considered explicitly by the kMC method while others are considered via the continuum model. This work applies a quasi-steady-state assumption (QSSA) within kMC for species not considered explicitly by the kMC model. The theoretical background for the application of QSSA in stochastic systems is given by Rao et al.<sup>33</sup> The concentration of those species on the surface is assumed to be in steady state within one kMC simulation time interval and thus only changes in between iterations. The probability of a species on a surface site is approximated by a conditional expectation based on the deterministic solution of the macroscopic equations.

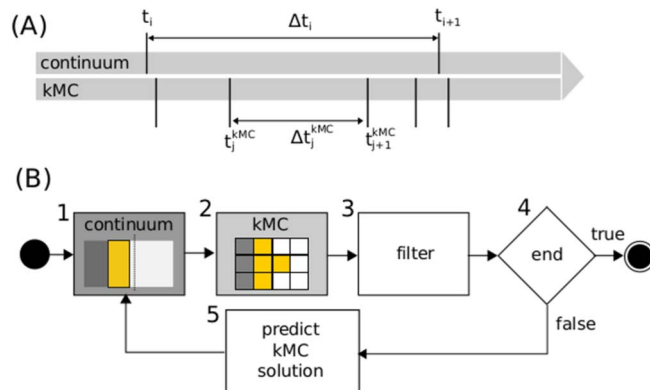


Figure 2. Time parallelization (A) and multi-scale algorithm (B).

**Multi-scale coupling.**—The main methodology, algorithms, and considerations of the multi-scale coupling are given here. The macroscopic model and the atomistic model are dynamically coupled by a multi-scale algorithm. The coupling is performed directly by sequentially performing kMC and continuum simulations and exchanging information about continuum and kMC states within a time interval.

The parallelization of both computations is shown in Figure 2. In Figure 2B the basic steps of the multi-scale simulation procedure is shown, while a multi-scale iteration is considered as a sequence of a continuum and a kMC simulation. In Step 1 the macroscopic model simulates up to a certain predefined time  $t_{i+1} = t_i + \Delta t_i$ , while time steps and their parallelization is shown in Figure 2A. After the iteration of the continuum model is finished, boundary conditions of the atomistic model are set to the values determined by the macroscopic model at  $t = t_{i+1}$ , which is the simplest approximation of the system state and is feasible as long as the system state change is small or iteration time steps are short. In Step 2, kMC simulation is performed until time in the kMC model  $t^{\text{kMC}}$  reaches  $t_{i+1}$ . If the final condition (e.g. cutoff potential) is not reached then the next multi-scale iteration is started, otherwise the overall simulation is terminated in Step 4. KMC results are used to determine parameters of the continuum system at the time  $t = t_i + \frac{\Delta t_i}{2}$ . The parameters depend on the present state of the kMC model and thus are time dependent parameters. Further, the stochastic nature of the kMC model leads to fluctuations in the parameters. Therefore, data filters are applied to smooth the output of the atomistic model in Step 3.<sup>34</sup> The smoothed output is used in Step 5 to predict the parameters of the following multi-scale iteration and is provided as continuous time dependent function to the macroscopic model.

This multi-scale coupling allows the coupling of detailed heterogeneous surface film growth mechanisms with the continuum model. The continuum model thereby applies mass balance equations, which contains net reaction rates based on kMC rates  $Q^{\text{kMC}}$ , which are determined as

$$Q^{\text{kMC}} = \frac{\Delta n}{\Delta t_i A^{\text{kMC}}} \quad [17]$$

where  $\Delta n$  is the total moles converted during simulation period  $\Delta t_i$  at the surface area  $A^{\text{kMC}}$ . To improve stability of the numerical solution, the rates  $Q$  of the continuum model were not directly set to rates of the kMC model, but instead the main impact of potential difference  $\Delta\Phi$  and layer thickness  $\delta$  was considered in the macroscopic model by

$$Q = \lambda^{\text{kMC}} \exp\left(\frac{0.5\Delta\Phi_{a,s^*} F - \delta \bar{E}_{\text{SEI}}^A}{RT}\right) \quad [18]$$

which is then corrected in every iteration by an adjustable parameter  $\lambda^{\text{kMC}}$  to fit rates of the kMC simulation. Further, the time step of a multi-scale iteration is adapted based on the kMC steps of the previous iteration. A low number of kMC steps in the previous iteration

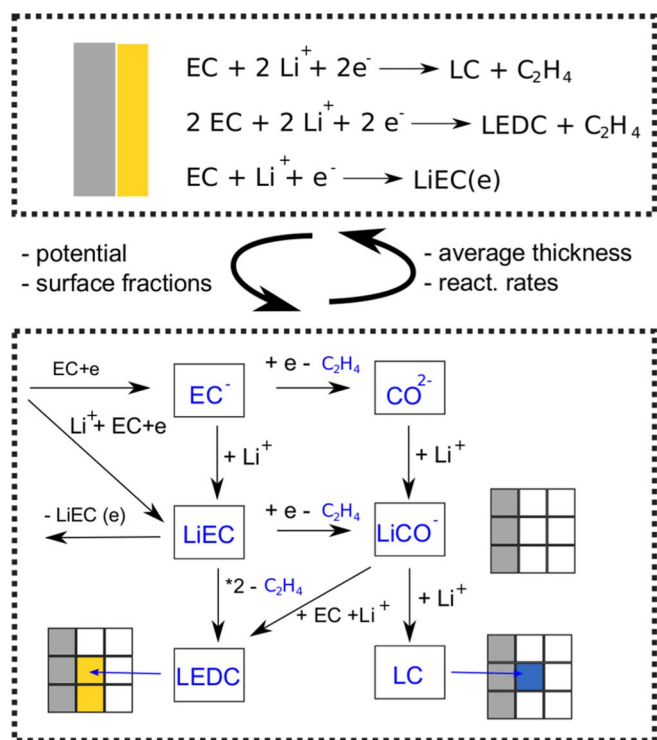


**Figure 3.** Illustration of the assumed reaction mechanism in the continuum model (top) and the kMC model (bottom) including information exchanged to synchronize those reactions in the multi-scale simulations.

step increases the length of the next time step. Dependent on the particular simulation, the robustness of the multiscale model can be sensitive on coupling strategy, such as iteration time step and data filter type.<sup>34</sup> The whole code including macroscopic and atomistic model is implemented in MATLAB. Partial differential equations are solved by the finite volume method and adaptive ODE solvers.

**Example problem: SEI layer formation in ethylene carbonate electrolyte.**—To demonstrate the capability of the multiscale model to analyze layer growth and its interaction with the macroscopic states, simulations are performed for an example problem. The decomposition of EC at a graphite electrode surface is chosen. The reaction mechanism is built on literature findings. As the mechanism is still

under discussion, it should be seen as an example, which can be adjusted later, once the full mechanism is known. The mechanism as implemented in the macroscopic and atomistic model is illustrated in Figure 3. Details about the concept as well as assumed surface film components and reactions are given below.

**Concept.**—The implemented reaction mechanism is shown in Table I along with the respectively applied simulation methods and kinetic parameters. Properties of the species involved in the kMC and continuum model are shown in Tables II and III, respectively. In the continuum model, species can be located in different phases, which is indicated in brackets for anode (*a*), anode surface film (*s*), adsorption film at the interface to the electrolyte (*s\**), and electrolyte (*e*). In the kMC model, the species Li<sup>+</sup>, EC, PF<sub>6</sub><sup>-</sup>, and e<sup>-</sup> are not considered explicitly, but occupy free surface sites with a certain probability as explained in Atomistic scale section. The intermediate species are initially generated on the surface via reactions of those species, i.e., reactions 1 and 2. When generated, intermediate species may diffuse on the surface, while probability of a diffusion step depends on the binding to its nearest solid neighbors. An essential prerequisite to obtain experimentally observed nano-structures is that reactions need to be favored differently depending on the local surface configuration. A physical reason for these differences may be a selective binding of species to certain solid components. We assume that intermediate LiC<sub>3</sub>H<sub>4</sub>O<sub>3</sub> and LiCO<sub>3</sub><sup>-</sup> have only low binding energies to the solid lithium carbonate (LC) and lithium ethylene dicarbonate (LEDC), respectively, which leads to the formation of such heterogeneous structures on the surface. The concentration of intermediate species in the electrolyte is negligible compared to salt and solvent concentration, and is set to zero.

As can be seen in Figure 3, net reactions considered in the continuum model are direct pathways from the reactants EC, Li<sup>+</sup>, and e<sup>-</sup> to the products C<sub>2</sub>H<sub>4</sub>, LC, LEDC, and the desorbed intermediate species LiC<sub>3</sub>H<sub>4</sub>O<sub>3</sub> (LiEC). To specify flow rates *Q*, the parameter λ<sup>kMC</sup> as well as average film thickness is provided by the kMC model. Continuous change of system states is considered via modeling surface fractions θ of the reactants Li<sup>+</sup>, PF<sub>6</sub><sup>-</sup>, and EC as well as electric potential ΔΦ<sub>*a,s\**</sub> by the continuum model.

**Solid components.**—The assumed solid products are LC and LEDC, which have been reported as being the main SEI film components.<sup>6,7,12,31,35,36</sup> LC is reported to be the most important component for SEI functionality<sup>13,37</sup> and formed with EC-based electrolytes.<sup>7</sup> A two-layer structure of the SEI is commonly reported,<sup>13,38</sup> with a dense inner film and a porous outer film.<sup>38</sup> In this work, a kMC model is used for the growth mechanism of the dense

**Table I.** Reaction processes including reaction rate constant *k*, Gibbs free energy Δ*G*<sup>0</sup>, and activation energy *E*<sup>A</sup>.

Number	Reactions	<i>k</i> [s <sup>-1</sup> ]	<i>E</i> <sup>A</sup> [kJ mol <sup>-1</sup> ]	α	method
1	C <sub>3</sub> H <sub>4</sub> O <sub>3</sub> + e <sup>-</sup> ⇌ C <sub>3</sub> H <sub>4</sub> O <sub>3</sub> <sup>-</sup>	5 × 10 <sup>12</sup>	65.27 <sup>12</sup>	0.5	kMC
2	C <sub>3</sub> H <sub>4</sub> O <sub>3</sub> + e <sup>-</sup> + Li <sup>+</sup> ⇌ LiC <sub>3</sub> H <sub>4</sub> O <sub>3</sub>	5 × 10 <sup>12</sup>	42.68 <sup>12</sup>	0.5	kMC
3	C <sub>3</sub> H <sub>4</sub> O <sub>3</sub> <sup>-</sup> + e <sup>-</sup> ⇌ CO <sub>3</sub> <sup>2-</sup> + C <sub>2</sub> H <sub>4</sub>	5 × 10 <sup>12</sup>	275.31 <sup>12</sup>	0.5	kMC
4	LiC <sub>3</sub> H <sub>4</sub> O <sub>3</sub> + e <sup>-</sup> ⇌ LiCO <sub>3</sub> <sup>-</sup> + C <sub>2</sub> H <sub>4</sub>	5 × 10 <sup>12</sup>	53 (chosen)	0.5	kMC
5	C <sub>3</sub> H <sub>4</sub> O <sub>3</sub> <sup>-</sup> + Li <sup>+</sup> ⇌ LiC <sub>3</sub> H <sub>4</sub> O <sub>3</sub>	1 × 10 <sup>13</sup>	40 (chosen)	–	kMC
6	CO <sub>3</sub> <sup>2-</sup> + Li <sup>+</sup> ⇌ LiCO <sub>3</sub> <sup>-</sup>	1 × 10 <sup>13</sup>	40 (chosen)	–	kMC
7	2 LiC <sub>3</sub> H <sub>4</sub> O <sub>3</sub> → (CH <sub>2</sub> OCO <sub>2</sub> Li) <sub>2</sub> + C <sub>2</sub> H <sub>4</sub>	1 × 10 <sup>13</sup>	5 (chosen)	–	kMC
8	LiCO <sub>3</sub> <sup>-</sup> + Li <sup>+</sup> + C <sub>3</sub> H <sub>4</sub> O <sub>3</sub> → (CH <sub>2</sub> OCO <sub>2</sub> Li) <sub>2</sub>	1 × 10 <sup>13</sup>	80 (chosen)	–	kMC
9	LiCO <sub>3</sub> <sup>-</sup> + Li <sup>+</sup> → Li <sub>2</sub> CO <sub>3</sub>	1 × 10 <sup>13</sup>	70 (chosen)	–	kMC
10	Li( <i>a</i> ) ⇌ V( <i>a</i> ) + Li <sup>+</sup> ( <i>s</i> ) + e <sup>-</sup> ( <i>a</i> )	1 × 10 <sup>13</sup>	30	0.5	continuum
11	Li <sup>+</sup> ( <i>s</i> ) ⇌ Li <sup>+</sup> ( <i>s*</i> )	1 × 10 <sup>13</sup>	30	–	continuum
12	Li <sup>+</sup> ( <i>s*</i> ) ⇌ Li <sup>+</sup> ( <i>e</i> )	1 × 10 <sup>13</sup>	30	0.5	continuum
13	PF <sub>6</sub> <sup>-</sup> ( <i>s*</i> ) ⇌ PF <sub>6</sub> <sup>-</sup> ( <i>e</i> )	1 × 10 <sup>13</sup>	30	0.5	continuum
14	C <sub>3</sub> H <sub>4</sub> O <sub>3</sub> ( <i>s*</i> ) ⇌ C <sub>3</sub> H <sub>4</sub> O <sub>3</sub> ( <i>e</i> )	1 × 10 <sup>13</sup>	30	–	continuum
15	2 C <sub>3</sub> H <sub>4</sub> O <sub>3</sub> ( <i>s*</i> ) + 2 Li <sup>+</sup> ( <i>s*</i> ) + 2 e <sup>-</sup> ( <i>s*</i> ) → (CH <sub>2</sub> OCO <sub>2</sub> Li) <sub>2</sub> + C <sub>2</sub> H <sub>4</sub> ( <i>e</i> )	kMC input	–	–	continuum
16	C <sub>3</sub> H <sub>4</sub> O <sub>3</sub> ( <i>s*</i> ) + 2 Li <sup>+</sup> ( <i>s*</i> ) + 2 e <sup>-</sup> ( <i>s*</i> ) → Li <sub>2</sub> CO <sub>3</sub> + C <sub>2</sub> H <sub>4</sub> ( <i>e</i> )	kMC input	–	–	continuum
17	C <sub>3</sub> H <sub>4</sub> O <sub>3</sub> ( <i>s*</i> ) + Li <sup>+</sup> ( <i>s*</i> ) + e <sup>-</sup> ( <i>s*</i> ) → LiC <sub>3</sub> H <sub>4</sub> O <sub>3</sub> ( <i>e</i> )	kMC input	–	–	continuum

**Table II. Standard chemical potential  $\mu^0$ , surface diffusion coefficient  $D$ , binding energy  $J_i$  to solid  $i$  in kJ/mol, and desorption rate constant  $k^{\text{des}}$  as used in the kMC model.**

Species	$\mu^0$ [kJ mol <sup>-1</sup> ]	$J_{\text{LC}}; J_{\text{LEDC}}; J_a$ [kJ mol <sup>-1</sup> ]	$k^{\text{des}}$ [s <sup>-1</sup> ]
C <sub>3</sub> H <sub>4</sub> O <sub>3</sub>	0	–	–
PF <sub>6</sub> <sup>-</sup>	0	–	–
Li <sup>+</sup>	10	–	–
e <sup>-</sup>	0	–	–
C <sub>3</sub> H <sub>4</sub> O <sub>3</sub> <sup>-</sup>	-33.93	22; 22; 22	–
CO <sub>3</sub> <sup>2-</sup>	256.44	22; 22; 22	–
LiC <sub>3</sub> H <sub>4</sub> O <sub>3</sub>	-574.63	8; 27; 29	$5 \times 10^7$
LiCO <sub>3</sub> <sup>-</sup>	-780.48	27; 3; 29	–
C <sub>2</sub> H <sub>4</sub>	0	5; 5; 5	$5 \times 10^7$
(CH <sub>2</sub> OCO <sub>2</sub> Li) <sub>2</sub>	-1386.91	–	–
Li <sub>2</sub> CO <sub>3</sub>	-1399	–	–

inner film. The outer porous film is considered by assuming all desorbed intermediates will react in the electrolyte and form solid components. Those solids will reduce the porosity of the electrode, which will impact macroscopic transport processes in the porous electrode during operation of the battery. During formation process, only very low currents are applied and thus spacial distribution of solvent and lithium due to transport processes in the porous electrode are neglected.

The size of the lattice elements in the kMC model is determined based on LC, which is a good lithium-ion conductor and therefore the most relevant surface species.<sup>31</sup> LC forms a crystal structure with a monoclinic lattice system with  $a = 8.370$  Å,  $b = 4.929$  Å,  $c = 5.870$  Å, and  $\beta = 117.1^\circ$ .<sup>31</sup> A cubic lattice would achieve the same volume with lateral length of  $a = 5.996 \approx 6$  Å. Thus the distance between lattice sites is defined to be  $\Delta L = 6 \times 10^{-10}$  m. The organic solid LEDC is reported to be the most common product observed in the SEI experimentally.<sup>12,39</sup> This species consists of two CH<sub>2</sub>OCO<sub>2</sub>Li groups, each of which are approximately as large as LC. Therefore, LEDC is assumed to fill two surface sites and has the same height as LC. This assumption enables the representation of the complex film structure in a simple cubic lattice.

**Reactions.**—The heterogeneous reaction mechanism applied here is abstracted from the literature. EC (C<sub>3</sub>H<sub>4</sub>O<sub>3</sub>) is reported to break down by consuming an electron through the breakage of one of the C–O bonds next to the C<sub>2</sub>H<sub>4</sub> group to form C<sub>3</sub>H<sub>4</sub>O<sub>3</sub><sup>-</sup> via reaction 1.<sup>6,10,12</sup> An alternative transition state for the bond breakage is suggested by,<sup>12</sup> where the energy barrier is lower in the presence of lithium, leading to the intermediate product LiC<sub>3</sub>H<sub>4</sub>O<sub>3</sub> via reaction 2. The reduced species C<sub>3</sub>H<sub>4</sub>O<sub>3</sub><sup>-</sup> and LiC<sub>3</sub>H<sub>4</sub>O<sub>3</sub> can then react with a further electron to form CO<sub>3</sub><sup>2-</sup> via reaction 3 and LiCO<sub>3</sub><sup>-</sup> via reaction 4, respectively. In both reactions, the gaseous species C<sub>2</sub>H<sub>4</sub> is

**Table III. Standard chemical potential  $\mu^0$  in kJ/mol and standard concentration  $C^0$  in mol/m<sup>3</sup>.**

Species	$\mu^0$ [kJ mol <sup>-1</sup> ]	$C^0$ [mol m <sup>-3</sup> ]
Li( <i>a</i> )	-11.65 <sup>25</sup>	$C_{\text{max}}$
e <sup>-</sup> ( <i>a</i> )	0	1
V( <i>a</i> )	0	$C_{\text{max}}$
Li <sup>+</sup> ( <i>s</i> )	–	1000
Li <sup>+</sup> ( <i>s</i> <sup>*</sup> )	10	$\Gamma/\sigma$
PF <sub>6</sub> <sup>-</sup> ( <i>s</i> <sup>*</sup> )	0	$\Gamma/\sigma$
V( <i>s</i> <sup>*</sup> )	-1	$\Gamma/\sigma$
C <sub>3</sub> H <sub>4</sub> O <sub>3</sub> ( <i>s</i> <sup>*</sup> )	0	$\Gamma/\sigma$
Li <sup>+</sup> ( <i>e</i> )	0	1200
PF <sub>6</sub> <sup>-</sup> ( <i>e</i> )	0	1200
C <sub>3</sub> H <sub>4</sub> O <sub>3</sub> ( <i>e</i> )	0	15000

**Table IV. Other model parameters.**

Parameter	value
Maximum concentration in the solid, $c_{\text{max}}$ [mol m <sup>-3</sup> ]	16100
temperature, $T$ [K]	300
solid diffusion coefficient, $D_a^{\text{Li}}$ [m <sup>2</sup> s <sup>-1</sup> ]	$1 \times 10^{-14}$
electrical resistivity of SEI, $\rho_{\text{SEI}}$ [ $\Omega$ m]	$5 \times 10^5$
double layer capacitance at anode/SEI interface, $C_{a,s}^{\text{DL}}$ [F m <sup>-2</sup> ]	0.2
double layer capacitance at SEI adsorption site/electrolyte interface, $C_{s^*,e}^{\text{DL}}$ [F m <sup>-2</sup> ]	10
active material volume fraction, $\epsilon_s$ [–]	0.58
concentration of Lithium ions in electrolyte, $c_e^{\text{Li}^+}$ [mol m <sup>-3</sup> ]	1200
start concentration of Lithium in solid $c_a^{\text{Li}}(0)$ [mol m <sup>-3</sup> ]	0
active material particle radius, $R_a$ [m]	$3 \times 10^{-6}, 10 \times 10^{-6}$
site-occupancy number, $\sigma$ [mol <sup>-1</sup> ]	$6.022 \times 10^{23}$
site density $\Gamma$ [m <sup>-2</sup> ]	$1/(\Delta L^2)$
C-ratio (based on concentration at 0 V) [–]	0.1
surface area roughness factor, $r_s$ [–]	5
kMC lattice size, $\Delta L$ [m]	$6 \times 10^{-10}$
cutoff voltage, $E_{\text{cut}}$ [V]	0
specific electron leakage activation energy, $\bar{E}_{\text{SEI}}^A$ [J m <sup>-1</sup> ]	$1 \times 10^{12}$
surface diffusion coefficient, $D$ [m <sup>2</sup> s <sup>-1</sup> ]	$1 \times 10^{-13}$

produced. For reaction 3, a transition state with a very high energy barrier is suggested.<sup>12</sup> Most literature agrees that CO<sub>3</sub><sup>2-</sup> quickly reacts further with lithium to form first LiCO<sub>3</sub><sup>-</sup> via reaction 6 and finally the solid LC (Li<sub>2</sub>CO<sub>3</sub>) via reaction 9.<sup>6,10-12,36,40,41</sup> Except for reaction 7, those reactions do not involve more than one of the rare intermediate species, therefore it can be expected that species C<sub>3</sub>H<sub>4</sub>O<sub>3</sub><sup>-</sup>, CO<sub>3</sub><sup>2-</sup>, and LiCO<sub>3</sub><sup>-</sup> have very short lifetimes, which indicates that desorption for those species does not need to be considered. LEDC ((CH<sub>2</sub>OCO<sub>2</sub>Li)<sub>2</sub>) is produced either through reactions 7 or 8. In reaction 7, LEDC is formed by the reaction of two LiC<sub>3</sub>H<sub>4</sub>O<sub>3</sub> and in reaction 8 with Li, EC, and LiCO<sub>3</sub><sup>-</sup>. Gibbs free energies of the reactions are partly provided by Wang et al.<sup>12</sup> Standard state chemical potentials and remaining reaction energies are chosen based on the data where applicable and otherwise chosen in the adequate order of magnitude. A quantitative computational determination of all parameters for this reaction mechanism via DFT simulations is yet not possible<sup>9</sup> and remains the subject of future studies. Additional parameters as applied in those simulations are summarized in Table IV.

As the parameters and mechanisms are not fully available in literature, the results should be considered as a first qualitative insight into the formation process and an assessment of the multiscale nature of SEI growth, and as a demonstration of the multiscale model as a way to evaluate hypothesized mechanisms.

## Results and Discussion

The multi-scale model is used to simulate the processes during the first charge for two cases that allow the assessment of the effect of electrodes with different macroscopic properties: particle size  $R_1 = 3$  μm, i.e. fine electrode, and  $R_2 = 10$  μm, i.e. coarse electrode. In both cases, formation is performed with typical low constant charge rate of 0.1 C. Detailed results for this process are shown and the effect of macroscopic properties on atomistic surface reaction and film growth and vice versa are discussed.

The potential of the graphite electrode during the first charging process is shown in Figure 4 and reveals the typical features of the formation process, such as the formation plateau at ~0.6 V, as well as the capacity needed for the first charge including the formation process. The slope of the potential is dependent on the particle size. The main differences between the curves can be explained as follows.

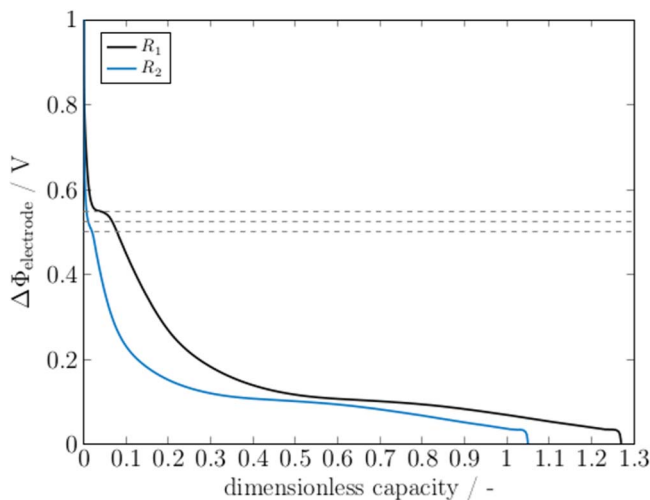


**Figure 4.** Electrode potential  $\Delta\Phi_{\text{electrode}}$  during the first charge of the formation process for electrodes with particle radius  $R_1 = 3 \times 10^{-6}$  m and  $R_2 = 10 \times 10^{-6}$  m. Dashed gray lines indicate the potentials 0.55 V, 0.525 V, and 0.5 V from top to bottom.

Smaller particles provide larger surface area so more solid electrolyte is formed, which results in a more distinct plateau at the beginning of charge and a higher capacity, i.e. lithium consumption, during the first charge. Furthermore, the formation process in the larger particle starts at lower potentials, which is due to higher overpotentials of the electron leakage process because of smaller surface area.

While it is possible to provide sound explanations for almost all of the main features that can be observed in the potential curve, it is more difficult to give explanations for the characteristics of the film growth, which is shown in Figure 5. This figure shows the average film thickness of both electrodes during the charging process for the dense inner film, which limits the passing of electrons. The figure does not include the intermediates desorbed to the electrolyte. Those species are instead expected to further react in the electrolyte phase and form a second porous film. This part of the SEI would affect diffusion processes in the porous electrode, but, due to very low charging rates, this effect is not further considered in this simulation. For both electrodes, the evolution of the film growth is qualitatively similar. While the growth is steep at the beginning of charging, the growth slows down at the end of charging. It has been stated that the film

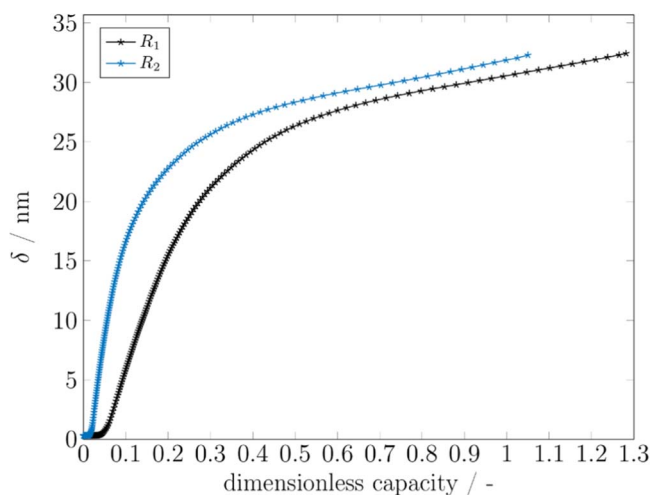


**Figure 5.** Thickness of the dense inner film during the first charge of the formation process for electrodes with particle radius  $R_1 = 3 \times 10^{-6}$  m and  $R_2 = 10 \times 10^{-6}$  m.

grows approximately with the square root of time,<sup>4,16</sup> which cannot be seen for the simulation results given here, but may be the long time trend for a life cycle test. In case of the electrode with large particles, the film grows faster compared to the electrode with small particles. This observation is again related to the smaller surface area provided by larger particles, which leads to much higher local surface current density and thus faster formation of the surface film. This slope of film thickness is similar to the inverse of the potential for both electrodes, which indicates the strong impact of electrode potential on the film growth. Further, the thickness of surface film for both electrodes is almost the same at the end of discharge (0 V), even though the potential is reached at considerably different discharge capacities. The particle size impacts growth rate much more than final thickness. In addition, it can be seen that, at the very beginning of the charging, the film is not growing, while the electrode potential in Figure 4 during this period stagnates, i.e. shows the typical formation plateau. The potential starts to drop as soon as a stable dense inner film is formed, which limits further electrochemical side reactions. Further detailed explanation is given later in the discussion.

The heterogeneous film structure and its growth are shown in Figure 6 for both electrodes at the same potentials. In both systems, LC and LEDC solids are the main products, while a nano-structuring of the solids can be observed. The structuring is a direct consequence of the different binding energies of the intermediates. The surface film shows some extent of roughness, but there are no areas with local heights that considerably deviate from the average film thickness. The reason for this observation is that resistance of the electrochemical side reactions is evaluated locally. Therefore, electrochemical processes have a higher probability to occur at regions close to the anode surface, which leads to an intrinsic adjustment of the local film thickness. If only some of the solid components allow electron leakage through the surface film, locally diverging growth rates can lead to less planar surfaces. However, those effects were not considered in this study.

In the following, the structure and the growth process for coarse and fine electrodes, which is shown in Figure 6 is discussed. The formation of the solid film starts at higher potentials with the fine electrode, which can be seen in Figures 6ABC and 6EFG and also in Figure 5. This can be explained by the difference in surface area, which leads to lower overpotentials of side reactions and lower surface fraction of intermediate reactants on the surface. The consequential higher potential of the formation plateau with fine electrodes results in the observed difference. Nevertheless it should be noted that the capacity where surface film growth starts is higher with the fine electrode, which can be seen in Figure 5. At the end of charge, i.e. 0 V (Figures 6DH), it again can be seen that final film thickness is almost independent of particle size. For both electrodes at the beginning of the formation process, several islands are formed at the anode surface, which then further grow until the whole surface is covered. It can be seen that LC and LEDC components are formed close to each other, while LEDC is located in the center and LC is at the edges of the islands. At the beginning of the formation, i.e. Figures 6AF, 6LC can be also observed detached from LEDC, while LEDC seems to grow only on top or next to LC components. This observation can be explained by reaction 7, where LEDC is formed by two  $\text{LiC}_3\text{H}_4\text{O}_3$  components on the surface. The probability for two of those species being next to each other is higher at regions where they bind to several solids than on the initially plain surface where they only bind to one solid component. Further, the different surface area with different particle size can influence the initial formation of islands. The surface fraction of intermediate is higher for coarse electrodes and results in high density of initial seeds as can be seen in Figure 6F. Comparing the final structure of both electrodes in Figures 6DH, it can be seen that the structures differ. However, these differences rather correlate to the stochastic nature of the process than to a significant impact of particle size. This may be due to low C-rates of the formation process and could be more distinct for faster formation procedures or during operation of the cell. No considerable impact of particle size on SEI structure could be observed in this simulation study.

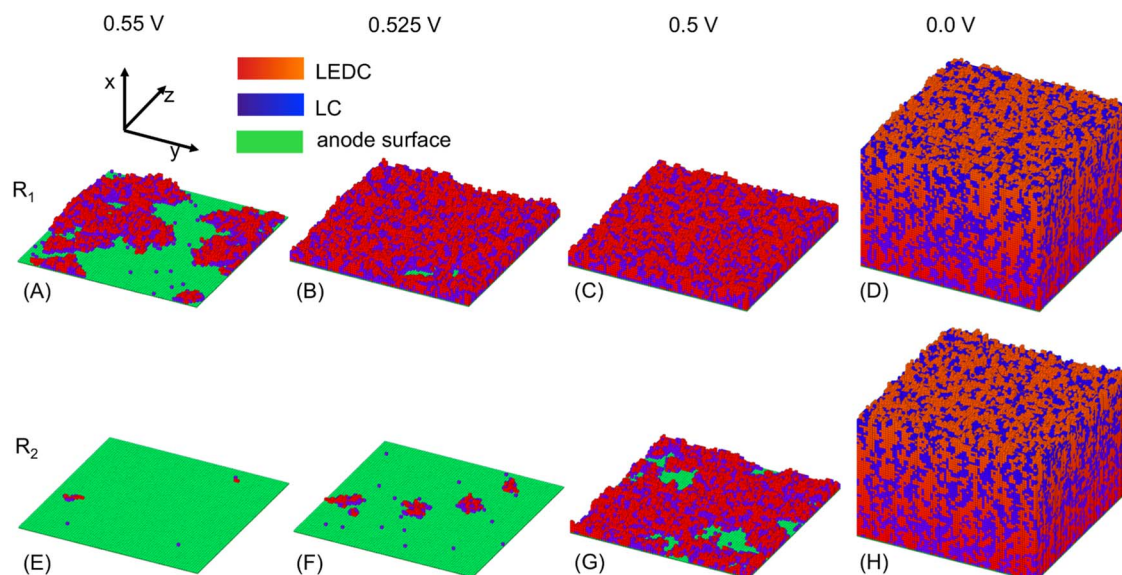


**Figure 6.** KMC configurations of the dense surface film for electrode with particle radius  $R_1 = 3 \times 10^{-6}$  m (A–D) and  $R_2 = 10 \times 10^{-6}$  m (E–H) at different electrode potentials with 0.55 V (A,E), 0.525 V (B,F), 0.5 V (C,G), and 0.0 V (D,H) during the first charge of the formation process.

Even if the final SEI structure is not significantly influenced by the particle size, a significant difference in the overall amount of the produced SEI components vs. total electrode volume can be observed in Figure 7. Comparing the volume fraction of electrode with small particles  $R_1$  and large particles  $R_2$  shows that about 5 times more SEI components have been formed for electrodes with small particles, which correlates also to the higher charge capacity in Figure 4, which is about 5% and 25% of the theoretical capacity for small and large particles, respectively. In both electrodes, the amount of porous SEI formed is about 2 times that of the dense SEI, i.e. LC and LEDC. For the cell with small particles, the fraction of solid components produced is very high and thus would considerably affect electrode performance during operation with higher C-rates.

The process rates for LEDC, LC, and desorption (des) at the surface are shown in Figure 8 for the kMC (marks) and the macroscopic model (lines). The rates are in good agreement, which is an indicator for good quality of the coupling. Comparing the quantity of the rates, the local reaction rates are seen to be considerably higher for the larger particles (B) compared to smaller particles (A), which is mainly due to the difference in surface area. For both electrodes, first the rate for intermediates desorbing increases rapidly, which is then followed with a delay by the actual production of the LEDC and LC component forming the dense inner film. For both electrodes, the rate of LEDC is higher compared to the rate of LC. As soon as the film covers the

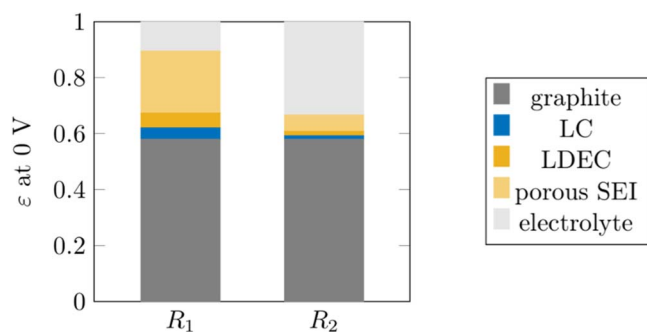


**Figure 7.** Volume fraction of electrode component at the end of charge, i.e. 0.0 V (A) for electrodes with particle radius  $R_1 = 3 \times 10^{-6}$  m and  $R_2 = 10 \times 10^{-6}$  m (B).

whole surface, the desorption rate decreases, which can be explained by the change of the surface properties from a flat ground to a rough film. A rough structure provides more binding energy for the intermediate components, which increases the probability of the following reactions. With ongoing film growth, reaction and desorption rates decrease due to a higher activation energy for the electron leakage

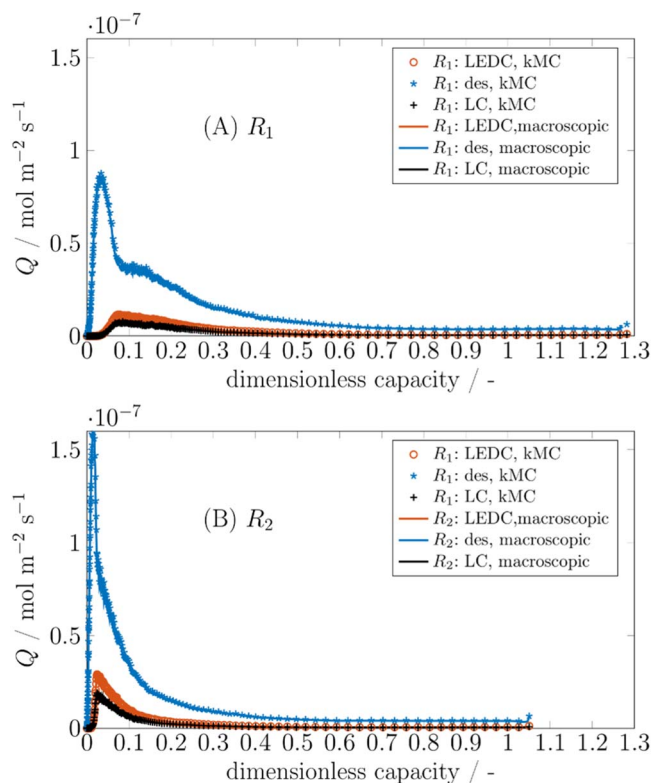


**Figure 8.** Reaction rates for LEDC, LC, and desorption (des) at the surface for electrode with particle radius  $R_1 = 3 \times 10^{-6}$  m (A) and  $R_2 = 10 \times 10^{-6}$  m (B) including the results of the macroscopic (lines) and the kMC simulation (marks).

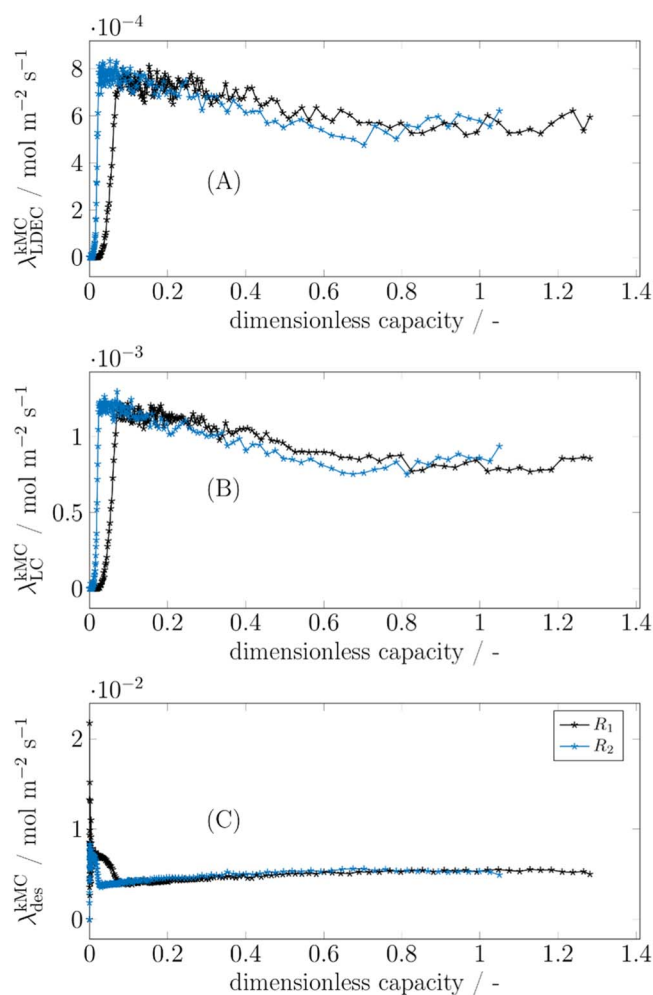


**Figure 9.** KMC output for calculation of reaction rates of LEDC (A), LC (B), and desorbed intermediates (D) for electrodes with small particles (black) and large particles (blue).

as applied for electrochemical side reactions. This decrease of film growth reactions is faster and steeper for large particles ( $R_2$ ). Further, for smaller particles this decrease is considerably slower in the beginning, which cannot be observed for the large particles. The magnitude of all three side reactions is similar in this simulation. For the LC rate in the beginning of charge, a steep overshooting can be observed for large particles, which is considerably more flattened for small particles. Even so, the general trend is similar for both electrodes, and it can be seen that the macroscopic properties considerably impacts the local reaction rates at the surface during the formation process.

To further understand the presented results and multi-scale coupling, the data exchanged between the models are analyzed. As explained previously, the reaction rates in the macroscopic model are not set directly to those determined by the kMC model. Instead reaction rates are defined in equation 18 and adjusted to fit reaction rates of the kMC model. The only adjustable parameter in this equation is  $\lambda^{\text{kMC}}$  for reaction 15–17, which is determined after each multi-scale iteration and thus represents the information actually passed from the atomistic to the macroscopic model. Figure 9 shows the parameter  $\lambda^{\text{kMC}}$  for reactions 15–17. For all three processes, fluctuations of this parameter can be seen. Fluctuation of the kMC output indicates the uncertainty of a process, which is strongly related to its frequency. As long as a process occurs frequently, statistics are reliable and fluctuation is low. The fluctuation may be decreased by increasing surface area  $A^{\text{kMC}}$ , but with an increase in computational time. As can be seen, all transferred parameters change during the formation process.

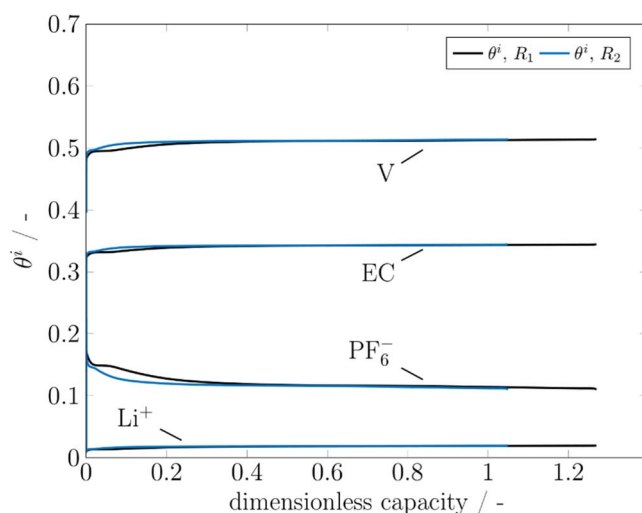


**Figure 10.** Surface fraction of major species at the adsorption film for electrodes with small particles (black) and large particles (blue). The states are calculated by the macroscopic model and fed to the atomistic model.

The parameter for the rate equation of LEDC is shown in Figure 9A. The value rapidly increases at the beginning of the formation process and then only slightly changes, while changes are higher with higher potential gradients. In Figure 9B, the parameter for rate equation of LC reaction is shown, which is qualitatively comparable to that of LEDC. In Figure 9C, the parameter for the rate equation of the desorption of  $\text{LiC}_3\text{H}_4\text{O}_3$  is seen to rapidly decrease as soon as a stable dense inner film is formed. This decrease starts earlier for the larger particles. Further, the value is seen to change during the whole charging process. In general, a change of these parameters denotes a correction of assumed dependencies of equation 18. A constant value would denote that there is no multi-scale interaction from atomistic to the macroscopic model. For the mechanisms shown, the assumed dependency of reaction rate from electrode potential and average film thickness seems to be good at the later state of the charge process, but not for the first part of the charging where the structure of the surface film, e.g. roughness, undergoes considerable changes.

The surface fractions provided by the macroscopic model are shown in Figure 10. The system states passed from macroscopic to the atomistic model are the surface fractions of the species ( $\text{Li}^+$ ,  $\text{PF}_6^-$ , EC, and vacancies V) as well as the electrode potential gradient  $\Delta\Phi_{a,s^*}$  between the anode  $a$  and the adsorption site  $s^*$ . The surface fractions of these species are very similar for both structures, because they mainly depend on the concentrations in the electrolyte, which is constant in this simulation. The most influential exchanged state is the electrode potential, which is shown in Figure 4. The electrode potential directly impacts all the electron-involving reactions on the surface, and is the variable that triggers and determines the multi-scale interaction between the macroscopic and the atomistic model. Through the electrode potential, the macroscopic conditions directly impact the evolution of the atomistic system, i.e. surface film growth and structure. The structure of the surface film determines the rate constants, i.e. electron consumption rates, as used in the macroscopic model and thus impacts the evolution of macroscopic properties such as electrical potential or average film resistance. Both lead to a continuous multi-scale interaction between the macroscopic and the atomistic model.

## Conclusions

This article introduces a multi-scale model for simulation-based analysis of SEI formation in lithium-ion batteries. The model dynamically couples a macroscopic electrode model including electron leakage limitation through a surface film with a kinetic Monte Carlo

model for the simulation of atomistic degradation processes on the surface as well as heterogeneous film growth. Simulations are carried out on the example that assumes EC as solvent and  $\text{LiPF}_6$  as salt. Two different particle sizes were used to reveal the effect of different macroscopic system properties.

This multi-scale modeling approach enables the coupling of heterogeneous growth mechanisms with continuum models. The macroscopic properties directly impacted the atomistic processes where lateral interactions lead to formation of nano-structures on the surface that result in different macroscopic side reaction rates at the surface and thus affects the macroscopic system. Furthermore, the results provide some suggestions on functionality of surface film growth. The film growth is shown to be considerably faster with larger particles, while the final thickness of the electrode correlates to the electrode potential and thus is similar for both electrodes.

This work provides a computational tool for the testing of hypothesized mechanisms that can be compared with experimental data. The method enables new possibilities toward understanding, predicting, and optimizing SEI formation by adapting macroscopic properties, electrolyte composition, or charging strategies. Future studies should, as more is known about the mechanisms, allow the building of models that enable a quantitative insight and SEI formation control.

### Acknowledgment

The authors gratefully acknowledge the financial support of this work by the German Academic Exchange Service (DAAD), the MIT-Germany Seed Fund, and the Nds. Ministerium für Wissenschaft und Kultur of the State of Lower Saxony with the Graduiertenkolleg Energiespeicher und Elektromobilität Niedersachsen (GEENI).

### List of Symbols

$A^{\text{kMC}}$	lattice area of the kMC simulation [ $\text{m}^2$ ]
$a_j^\gamma$	activity of species $j$ in phase $\gamma$ [–]
$a_s$	surface area density [ $\text{m}^{-1}$ ]
$C_{\gamma}^{0,j}$	standard state concentration of species $j$ in phase $\gamma$ [ $\text{mol m}^{-3}$ ]
$C_{\gamma,\kappa}^{\text{DL}}$	double layer capacitance at the interface between phase $\gamma$ and $\kappa$ [ $\text{F m}^{-2}$ ]
$c_j^\gamma$	concentration of species $j$ in phase $\gamma$ [ $\text{mol m}^{-3}$ ]
$D$	surface diffusion [ $\text{m}^2 \text{s}^{-1}$ ]
$D_j^\gamma$	diffusion coefficient of species $j$ in phase $\gamma$ [ $\text{m}^2 \text{s}^{-1}$ ]
$E^A$	activation energy [ $\text{J mol}^{-1}$ ]
$F$	Faraday constant [ $\text{C mol}^{-1}$ ]
$\Delta G$	Gibbs free energy [ $\text{J mol}^{-1}$ ]
$J$	surface current density [ $\text{A m}^{-2}$ ]
$J_j^A$	binding energy to species $j$ [ $\text{J mol}^{-1}$ ]
$j$	current density [ $\text{A m}^{-3}$ ]
$k$	reaction rate constant [ $\text{s, mol, m}$ ]
$\Delta L$	distance between lattice sites [ $\text{m}$ ]
$N_{\nu,\gamma}^j$	flow of species $j$ between phase $\gamma$ and $\nu$ [ $\text{mol m}^{-2}$ ]
$n_j$	number of nearest neighbors of species $j$ [–]
$n_x$	number of lattice sites in $x$ direction [–]
$n_y$	number of lattice sites in $y$ direction [–]
$n^i$	mol number of solid $i$ [–]
$Q_i$	irreversible side reaction to solid $i$ [ $\text{mol m}^{-2}$ ]
$q$	process frequency [ $\text{s}^{-1}$ ]
$R$	ideal gas constant [ $\text{J mol}^{-1} \text{K}^{-1}$ ]
$R_a$	particle radius of anode [ $\text{m}$ ]
$r$	space variable in particle [ $\text{m}$ ]
$r_s$	roughness factor [–]
$T$	temperature [ $\text{K}$ ]
$t$	time [ $\text{s}$ ]

### Subscripts and Superscripts

$a$	anode
$s$	surface film
$s^*$	adsorption site of surface film
$e$	electrolyte
$\gamma$	a phase
$\nu$	a phase
SEI	Solid Electrolyte Interface
LC	lithium carbonate
LEDC	lithium ethylene dicarbonate
des	any solid in the porous SEI phase
eff	effective

### Greek

$\alpha_i$	symmetry factor of reaction $i$ [–]
$\delta$	average surface film thickness [ $\text{m}$ ]
$\Delta\Phi$	potential difference [ $\text{V}$ ]
$\varepsilon$	volume fraction [–]
$\mu^0$	standard state chemical potential [ $\text{J mol}^{-1}$ ]
$\Gamma$	site density [ $\text{m}^{-2}$ ]
$\rho$	electrical resistivity [ $\Omega \text{m}$ ]
$\sigma$	site-occupancy number [ $\text{mol}^{-1}$ ]
$\theta^j$	surface fraction of species $j$ [–]

### References

1. M. Winter, The Solid Electrolyte Interphase – The Most Important and the Least Understood Solid Electrolyte in Rechargeable Li Batteries, *Zeitschrift für Physikalische Chemie, International Journal of Research in Physical Chemistry and Chemical Physics*, **223**, 1395 (2009).
2. S. Chattopadhyay, A. L. Lipsion, H. J. Karmel, J. D. Emery, T. T. Fister, P. A. Fenter, M. C. Hersam, and M. J. Bedzyk, In Situ X-ray Study of the Solid Electrolyte Interphase (SEI) Formation on Graphene as a Model Li-ion Battery Anode, *Chemistry of Materials*, **24**, 3038 (2012).
3. S. J. An, J. Li, C. Daniel, D. Mohanty, S. Nagpure, and D. L. Wood, The state of understanding of the lithium-ion-battery graphite solid electrolyte interphase (SEI) and its relationship to formation cycling, *Carbon*, **105** 52 (2016).
4. M. B. Pinson and M. Z. Bazant, Theory of SEI Formation in Rechargeable Batteries: Capacity Fade, Accelerated Aging and Lifetime Prediction, *Journal of the Electrochemical Society*, **160**, A243 (2013).
5. P. Arora, R. E. White, and M. Doyle, Capacity Fade Mechanisms and Side Reactions in Lithium-Ion Batteries, *Journal of The Electrochemical Society*, **145**, 3647 (1998).
6. P. Ganesh, P. R. C. Kent, and D. E. Jiang, Solid-Electrolyte Interphase Formation and Electrolyte Reduction at Li-Ion Battery Graphite Anodes: Insights from First-Principles Molecular Dynamics, *Journal of Physical Chemistry C*, **116**, 24476 (2012).
7. P. Verma, P. Maire, and P. Novák, A Review of the Features and Analyses of the Solid Electrolyte Interphase in Li-Ion Batteries, *Electrochimica Acta*, **55**, 6332 (2010).
8. L. Seidl, S. Martens, J. Ma, U. Stimming, and O. Schneider, In-Situ Scanning Tunneling Microscopy Studies of the SEI Formation on Graphite Electrodes for Li+–Ion Batteries, *Nanoscale*, **1**, 14004 (2016).
9. K. F. Kalz, R. Kraehnert, M. Dvoyashkin, R. Dittmeyer, R. Gläser, U. Krewer, K. Reuter, and J.-d. Grunwaldt, Future Challenges in Heterogeneous Catalysis: Understanding Catalysts under Dynamic Reaction Conditions, *ChemCatChem*, **9**, 17 (2016).
10. K. Leung and J. L. Budzien, Ab Initio Molecular Dynamics Simulations of the Initial Stages of Solid-Electrolyte Interphase Formation on Lithium Ion Battery Graphitic Anodes, *Physical Chemistry Chemical Physics*, **12**, 6583 (2010).
11. K. Leung, Electronic Structure Modeling of Electrochemical Reactions at Electrode/Electrolyte Interfaces in Lithium Ion Batteries, *The Journal of Physical Chemistry C*, **117**, 1539 (2013).
12. Y. Wang, S. Nakamura, M. Ue, and P. B. Balbuena, Theoretical Studies to Understand Surface Chemistry on Carbon Anodes for Lithium-Ion Batteries: Reduction Mechanisms of Ethylene Carbonate, *Journal of the American Chemical Society*, **123**, 11708 (2001).
13. S. Shi, P. Lu, Z. Liu, Y. Qi, L. G. Hector, H. Li, and S. J. Harris, Direct Calculation of Li-Ion Transport in the Solid Electrolyte Interphase, *Journal of the American Chemical Society*, **134**, 15476 (2012).
14. S. Shi, Y. Qi, H. Li, and L. G. Hector, Defect Thermodynamics and Diffusion Mechanisms in  $\text{Li}_2\text{CO}_3$  and Implications for the Solid Electrolyte Interphase in Li-Ion Batteries, *Journal of Physical Chemistry C*, **117**, 8579 (2013).
15. R. N. Methekar, P. W. C. Northrop, K. Chen, R. D. Braatz, and V. R. Subramanian, Kinetic Monte Carlo Simulation of Surface Heterogeneity in Graphite Anodes for Lithium-Ion Batteries: Passive Layer Formation, *Journal of The Electrochemical Society*, **158**, A363 (2011).

16. H. J. Ploehn, P. Ramadass, and R. E. White, Solvent Diffusion Model for Aging of Lithium-Ion Battery Cells, *Journal of The Electrochemical Society*, **151**, A456 (2004).
17. E. Peled, Advanced Model for Solid Electrolyte Interphase Electrodes in Liquid and Polymer Electrolytes, *Journal of The Electrochemical Society*, **144**, L208 (1997).
18. A. M. Colclasure, K. A. Smith, and R. J. Kee, Modeling Detailed Chemistry and Transport for Solid-Electrolyte-Interface (SEI) Films in Li-Ion Batteries, *Electrochimica Acta*, **58**, 33 (2011).
19. M. A. Quiroga and A. A. Franco, A Multi-Paradigm Computational Model of Materials Electrochemical Reactivity for Energy Conversion and Storage, *Journal of the Electrochemical Society*, **162**, E73 (2015).
20. Z. Zheng, R. M. Stephens, R. D. Braatz, R. C. Alkire, and L. R. Petzold, A Hybrid Multiscale Kinetic Monte Carlo Method for Simulation of Copper Electrodeposition, *Journal of Computational Physics*, **227**, 5184 (2008).
21. F. Röder, R. D. Braatz, and U. Krewer, Multi-scale modeling of solid electrolyte interface formation in lithium-ion batteries, *Computer Aided Chemical Engineering*, **38**, 157 (2016).
22. K. Xu, Nonaqueous Liquid Electrolytes for Lithium-Based Rechargeable Batteries, *Chemical Reviews*, **104**, 4303 (2004).
23. S. Santhanagopalan, Q. Guo, P. Ramadass, and R. E. White, Review of Models for Predicting the Cycling Performance of Lithium Ion Batteries, *Journal of Power Sources*, **156**, 620 (2006).
24. F. G. Helfferich, Kinetics of Homogeneous Multistep Reactions, volume 38 of *Comprehensive Chemical Kinetics*, Elsevier Science Ltd, 2001.
25. A. M. Colclasure and R. J. Kee, Thermodynamically Consistent Modeling of Elementary Electrochemistry in Lithium-Ion Batteries, *Electrochimica Acta*, **55**, 8960 (2010).
26. T. O. Drews, R. D. Braatz, and R. C. Alkire, Coarse-Grained Kinetic Monte Carlo Simulation of Copper Electrodeposition with Additives, *International Journal for Multiscale Computational Engineering*, **2**, 313 (2004).
27. S. Pal and D. P. Landau, Monte Carlo Simulation and Dynamic Scaling of Surfaces in MBE Growth, *Physical Review B*, **49**, 10597 (1994).
28. J. D. Weeks and G. H. Gilmer, Dynamics of Crystal Growth, *Advances in Chemical Physics*, **40**, 157 (2007).
29. U. Burghaus (Ed.), A practical guide to kinetic Monte Carlo simulations and classical molecular dynamics simulations : an example book, Nova Science Publ., New York, 2006.
30. P. Lu and S. J. Harris, Lithium Transport Within the Solid Electrolyte Interphase, *Electrochemistry Communications*, **13**, 1035 (2011).
31. Y. C. Chen, C. Y. Ouyang, L. J. Song, and Z. L. Sun, Electrical and Lithium Ion Dynamics in Three Main Components of Solid Electrolyte Interphase from Density Functional Theory Study, *The Journal of Physical Chemistry C*, **115**, 7044 (2011).
32. M. T. Lawder, P. W. C. Northrop, and V. R. Subramanian, Model-Based SEI Layer Growth and Capacity Fade Analysis for EV and PHEV Batteries and Drive Cycles, *Journal of The Electrochemical Society*, **161**, A2099 (2014).
33. C. V. Rao and A. P. Arkin, Stochastic Chemical Kinetics and the Quasi-Steady-State Assumption: Application to the Gillespie Algorithm, *Journal of Chemical Physics*, **118**, 4999 (2003).
34. R. D. Braatz, R. C. Alkire, and E. G. Seebauer, Multiscale Modeling and Design of Electrochemical Systems, in: *Electrochemical Surface Modification – Thin Films, Functionalization and Characterization*, volume 10 of *Advances in Electrochemical Science and Engineering*, Wiley-VCH, Weinheim, Germany, 2008, pp. 289–334.
35. D. Aurbach, B. Markovsky, I. Weissman, E. Levi, and Y. Ein-Eli, On the Correlation between Surface Chemistry and Performance of Graphite Negative Electrodes for Li Ion Batteries, *Electrochimica Acta*, **45**, 67 (1999).
36. D. Aurbach, A Comparative Study of Synthetic Graphite and Li Electrodes in Electrolyte Solutions Based on Ethylene Carbonate-Dimethyl Carbonate Mixtures, *Journal of The Electrochemical Society*, **143**, 3809 (1996).
37. Y. Ein-Eli, B. Markovsky, D. Aurbach, Y. Carmeli, H. Yamin, and S. Luski, Dependence of the Performance of Li-C Intercalation Anodes for Li-ion Secondary Batteries on the Electrolyte Solution Composition, *Electrochimica Acta*, **39**, 2559 (1994).
38. A. M. Andersson and K. Edström, Chemical Composition and Morphology of the Elevated Temperature SEI on Graphite, *Journal of The Electrochemical Society*, **148**, A1100 (2001).
39. M. A. Kiani, M. F. Mousavi, and M. S. Rahmanifar, Synthesis of Nano- and Micro-Particles of LiMn<sub>2</sub>O<sub>4</sub>: Electrochemical Investigation and Assessment as a Cathode in Li Battery, *International Journal of Electrochemical Science*, **6**, 2581 (2011).
40. K. Xu, Y. Lam, S. S. Zhang, T. R. Jow, and T. B. Curtis, Solvation Sheath of Li<sup>+</sup> in Nonaqueous Electrolytes and its Implication of Graphite/Electrolyte Interface Chemistry, *Journal of Physical Chemistry C*, **111**, 7411 (2007).
41. K. Leung, Two-Electron Reduction of Ethylene Carbonate: A Quantum Chemistry Re-Examination of Mechanisms, *Chemical Physics Letters*, **568-569**, 1 (2013).